High Temperatures-High Pressures, Vol. 52, pp. 285–305
Reprints available directly from the publisher
Photocopying permitted by license only
DOI: 10.32908/hthp.v52.1409

Quantitative thermal investigation of a fayalite particle and a Si-rich layer in oxide scale formed on steel

YUTO SUGANUMA[1], SAORI SHINOHARA[2], YUTA INOUE[2], TSUYOSHI NISHI[1], HIROMICHI OHTA[1], HIROSHI TANEI[3], MASAHIRO SUSA[2] AND RIE ENDO[2,4]*

[1]*Graduate School of Science and Engineering, Ibaraki University, Hitachi, Ibaraki, 316-8511, Japan*
[2]*Department of Materials Science and Engineering, Tokyo Institute of Technology, Meguro-ku, Tokyo 152-8550, Japan*
[3]*Process Research Laboratories, Nippon Steel Corporation, 20-1 Shintomi, Futtsu, Chiba, 293-8511 Japan*
[4]*Department of Materials Science and Engineering, Shibaura Institute of Technology, Koto-ku, Tokyo 135-8548, Japan*

Received: December 26, 2022; Accepted: May 15, 2023.

Fayalite (Fe_2SiO_4) is a major component of olivine and is often formed in the surface oxide layer (oxide scale) on steel plates owing to its high-temperature oxidation. The thermal conductivity of the oxide scale and its constituents, including fayalite, is essential for controlling the cooling rate of hot steel plates. Therefore, this study uses modulated thermoreflectance microscopy to determine the thermal effusivity/conductivity of fayalite particles with diameters smaller than 180 μm because the sample commercially available is such a small size. This thermal optical microscopy enables the measurement of thermal effusivity for small areas, such as 10 μm. The thermal effusivity and conductivity were found to be 4.1 ± 0.2 $kJs^{-0.5}K^{-1}m^{-2}$ and 6.0 ± 0.5 $Wm^{-1}K^{-1}$, respectively. These values are representative of the bulk value. Additionally, the thermal conductivity of fayalite is shown to be higher than that of wüstite ($Fe_{1-x}O$), which is the main component of the oxide scale. The oxide scale formed on the thick steel plate comprises a Si-rich layer, a wüstite layer, and a magnetite layer. Furthermore, the Si-rich layer comprises fayalite, wüstite, and pores.

*Corresponding author: rie-endo@shibaura-it.ac.jp

The effective thermal conductivity of the Si-rich layer was calculated by observing the oxide scale formed on the steel plate. The low thermal conductivity of the Si-rich layer indicates that the thermal conductivity of the layer is strongly affected by the porosity of the oxide scale. Furthermore, although the Si-rich layer is thin, it significantly contributes to the heat resistance of the oxide scale.

Keywords: Thermal effusivity, thermal conductivity, fayalite, oxide scale, modulated thermoreflectance microscopy, hot-rolling process

1 INTRODUCTION

Fayalite (Fe_2SiO_4), which is one of the two constituents of olivine (general formula $(Mg, Fe)_2SiO_4$), is a well-known mineral found in the steelmaking process. The knowledge of the thermal conductivity of the olivine group is essential for the steelmaking process or future lunar utilization, as this value can be used for the thermal design of spacecraft and buildings. However, to date, values of the thermal conductivity of fayalite have only been reported for its sintered form [1] and fayalite-rich olivine [2, 3].

In steelmaking, fayalite is formed in the surface oxide layer (oxide scale) of steel plates. Steel usually contains Si; for example, high-strength steel used in automobiles and thick steel plates used in the construction of ships, bridges, and buildings. The presence of Si in iron results in forming of a Si-rich oxide layer comprising fayalite and wüstite ($Fe_{1-x}O$) with pores owing to the high-temperature oxidation of steel during the hot-rolling process. The Si-rich layer is located at the interface between the $Fe_{1-x}O$ scale, the main component of the oxide scale, and steel [4–7]. The knowledge of the thermal conductivity of the oxide scale is essential for optimizing the hot-rolling process, considering temperature control is important for producing high-quality steel. The oxide scale has a lower thermal conductivity than steel and offers thermal resistance when the plate is cooled. While many studies have reported the thermal conductivity of the $Fe_{1-x}O$ scale, which is the main component of the oxide scale, the thermal conductivity of the Si-rich oxide layer is still unknown owing to the lack of reliable values of the thermal conductivity of fayalite [8–13].

According to the phase diagram of the FeO-SiO_2 system [14], fayalite is a line compound. Hence, it is difficult to make bulk samples that are large enough for conducting conventional thermal conductivity measurements. Takeda *et al.* reported the thermal conductivity of sintered fayalite [1]. In this case, the effect of pores should be removed using a prediction formula to obtain the thermal conductivity of fayalite alone [15–17]. Therefore, it is necessary to choose a suitable equation according to the ratio and dispersion state of the pores. In other words, the thermal conductivity of the obtained fayalite varies depending on the equation chosen.

Several methods have been developed for the thermophysical property measurement of material small region, for example, the scanning thermal microscopy (SThM) and the thermal reflectance method. The SThM combines atomic force microscopy with a self-heated small probe as a heating source and sensor [18, 19]. The technique can be applied to low-dimensional nanomaterials, such as nanoparticles. On the other hand, the thermoreflectance method heats the sample surface with a laser (pump laser), and the temperature change of the sample surface is measured as the intensity change of the reflected laser (probe laser) [20]. The diameters of pump and probe lasers are in the orders of several tens of micrometers. Thus, the measured thermal property for the measured region is considered for the bulk. From the above aspects, this study chose modulated thermoreflectance microscopy, which is one of the thermoreflectance techniques, since the thermophysical property of the bulk is required.

Modulated thermoreflectance microscopy is a technique that enables the measurement of the thermal effusivity of areas as small as 10 μm [20–25]. This method can measure the thermal effusivity of fayalite particles larger than the resolution of the measurement. In the case of the fayalite particle being large enough to be considered bulk, the measured value of thermal effusivity can also be regarded as the value of the bulk material. Therefore, this study aimed to measure the thermal effusivity and thermal conductivity of fayalite particles using a thermal microscope. Based on the obtained thermal conductivity, the effect of the Si-rich layer on the effective thermal conductivity of the oxide scale was evaluated for the practical steel plate.

2 EXPERIMENT

2.1 Principle of modulated thermoreflectance microscopy

A thermal microscope called modulated thermoreflectance microscope (MDTR) combines the cyclic heating method with the thermoreflectance method to measure the thermal effusivity on the micrometer scale [20–25]. As shown in Fig. 1(a), a thin metallic film (Molybdenum (Mo) in this work) is deposited on the sample surface, which is periodically heated by an intensity-modulated heating laser (e.g., 808 nm). The sample surface exhibits a temperature change in response to the heating laser. At the sample surface, the temperature change has the same period as the heating laser but with a phase delay, which depends on the thermophysical properties of the sample. The change in surface temperature is measured by monitoring the intensity of the reflected light of a fixed-power detection laser (e.g., 655 nm). The optical setup shown in Fig. 1(b) is used to measure the corresponding phase difference.

The thermal effusivity of the sample is calculated based on the two-layer model for the Mo film and the sample from the measured phase difference. The model assumes that the sample is of semi-infinite thickness and that heat diffuses only in the direction of the thickness. The one-dimensional heat flow model can be applied when the thermal effusivity is smaller than about 5 $kJs^{-0.5}m^{-2}K^{-1}$, and the volumetric heat capacity (ρC, ρ: density, and C: specific heat) is larger than 2.5×10^6 $Jm^{-3}K^{-1}$. [23]. In the steady-state, the AC component of the temperature response $T(t)$ of a sample surface owing to cyclic heating (angular frequency ω) is expressed as:

$$T(t) = A\sin(\omega t - \delta) \tag{1}$$

where δ is the phase difference between the period of the temperature change of the Mo thin film and the intensity of the modulated heating laser, δ is expressed as:

$$\delta = \frac{3\pi}{4} + \arctan\left[\frac{\cosh^2\sqrt{\frac{\omega\tau_f}{2}}\left(\tanh\sqrt{\frac{\omega\tau_f}{2}} + \beta\right)\left(\tanh\sqrt{\frac{\omega\tau_f}{2}} + \beta^{-1}\right)}{\cos^2\sqrt{\frac{\omega\tau_f}{2}}(\beta - \beta^{-1})\tan\sqrt{\frac{\omega\tau_f}{2}}}\right] \tag{2}$$

where

$$\tau_f = \frac{{d_f}^2}{\alpha_f} \tag{3}$$

$$\beta = \frac{b_s}{b_f} \tag{4}$$

where d_f is the thickness of the Mo film, α_f is the thermal diffusivity of the Mo film, and b_s and b_f are the thermal effusivities of the sample and Mo film, respectively. The above equations determine the value of β to obtain b_s. It has been reported that the thermal effusivity of the sample can be determined through Eqs. (1) to (4) within the accuracy of 4%, where the thermal resistance has been neglected at the contact between the Mo film and the sample [22].

Thermal conductivity (λ) is calculated from the thermal effusivity as the following equation.

$$\lambda = b^2/\rho C \tag{5}$$

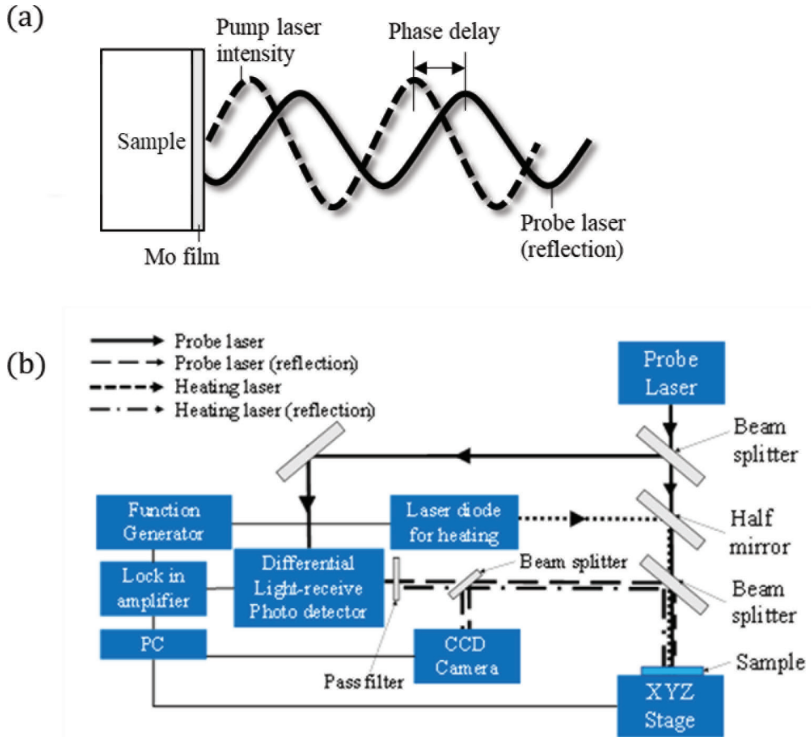

FIGURE 1
Schematic diagram of principle of the photothermal pump-probe measurement; (a) and opticals system with a modulated domain thermoreflectance microscope; (b).

2.2 Fayalite sample

The sample was fabricated from commercially available fayalite powder (particle size <180 μm). The phase identification of the sample was carried out using X-ray diffraction (XRD) before the experiment was conducted. A part of the fayalite sample was ground to perform the powder X-ray diffraction. The X-ray source used was Co-Kα. To prepare the sample for the thermal microscope measurements, large particles with a diameter of 150 μm or more are sieved. The selected particles are then placed in a container with a diameter of approximately 10 mm and filled with epoxy resin. The samples are then re-embedded in a 25.4 mm diameter container with a standard sample of fused silica. The surfaces of all pieces are polished to a mirror finish and further examined using thermal, optical, and scanning electron microscopies.

2.3 Thermal effusivity measurement conditions

For the thermal microscope measurements, a 100 nm thin film of Mo is formed on the mirror-polished sample surface via DC sputtering. The

measurements are carried out at room temperature (25 °C), and the sample is heated using an 830 nm wavelength semiconductor laser with a running intensity of 26 mW and a frequency of 1 MHz. Detection is performed using a He-Ne laser with a wavelength of 633 nm and a radiation intensity of 620 μW. The spot sizes of the heating and detection lasers are 27 and 8 μm, respectively.

First, a reference sample of fused silica is measured to obtain δ, and the thermal effusivity b_s and diffusivity α_f of the Mo thin film are determined to reproduce the thermal effusivity of fused silica (1.57 $kJs^{-0.5}m^{-2}K^{-1}$, [12]). By substituting Eq. (6) into Eq. (3), b_f can be determined using Eq. (2) as:

$$\alpha_f = \left(\frac{b_f}{\rho_f C_f} \right)^2 \tag{6}$$

The value used for $\rho_f C_f$ was 2.29×10^6 $Jm^{-3}K^{-1}$ [22].

Measurements of fayalite were first carried out every 10 μm of a 1000 × 1000 μm^2 area containing several fayalite particles. The sample surface is leveled and placed on the sample stage. At the starting position, the height of the sample stage was adjusted to focus on the sample surface. Measurements were performed at intervals of 10 times for 250 ms per position, and the average value was used as the thermal effusivity at that point. Ten measurements were performed in 500 ms per point, and the average value was taken as the value of δ at that point. By changing the sample stage along the Y direction again, the measurement was carried out every 10 μm in 1000 μm. Then, the sample stage returned to the initial position and moved 10 μm along the X direction; the measurements were conducted along the Y direction. This procedure was repeated 100 times to obtain mapping data of δ for 1000 × 1000 μm^2 area. After the experiment, the collected δ data were converted into thermal effusivity with the software Mathematica [26]. Subsequently, measurements were conducted by focusing on the individual particles using the MDTR technique. The heat diffusion length for the measurement was evaluated after deriving the thermal effusivity of the sample since the sample size was limited: particle size was 150–180 μm. The technique has then only been applied to particles with diameter larger than 20 μm. Samples were mounted in resin.

2.4 Characterization of oxide scale formed on thick steel plate

A commercial thick steel plate was analyzed to observe the Si-rich layer in the oxide scale formed on the plate. Table 1 shows the chemical composition of steel plate used in this study. For the sample preparation, the steel plate was cut into 15 × 15 mm^2 that was 2 mm thick and then filled with resin. Then, the sample was cut and polished to a mirror finish. Subsequently,

their cross-sections are examined using scanning electron microscopy (SEM).

TABLE 1
Chemical composition of steel plate used in this study (in mass%)

C	Si	Mn	P	S	Cu	Ni	Cr	Mo	Al	Fe
0.14	0.22	0.49	0.017	0.013	0.2	0.1	0.1	0.03	0.004	Bal.

3 RESULTS AND DISCUSSION

3.1 Determination of thermal effusivity of fayalite

Fig. 2(a) shows the XRD profile of the fayalite powder sample. It was confirmed that the phase present in the sample was only fayalite. Fig. 2(b) shows an SEM image of the fayalite sample. It can be seen that the particles are dispersed and exhibit angular shapes; some of which with equivalent diameters smaller than 180 μm. Additionally, internal cracks were observed in certain particles.

Figs. 3(a) and (b) show the results of the first thermal effusivity measurements and the backscattered electron image (BEI) obtained after the measurement, respectively. Thermal effusivity measurements were performed every 10 μm in the area demarcated by the square shown in Fig. 3(b). In the areas measured by MDTR shown in Fig. 3(a), the transparent regions of the measured area exhibit abnormally large values, *e.g.*, 0.1–1000 $MJs^{-0.5}m^{-2}K^{-1}$. This result was mainly observed for the resin. The lifting of the Mo film owing to heating might be responsible for the abnormally large values, considering the epoxy resin has a much smaller thermal conductivity (0.2 $Wm^{-1}K^{-1}$ [27]) compared to that of the sample particle (6 $Wm^{-1}K^{-1}$, calculated below). The applied power of the heating laser was adjusted for the sample particle; this power could be large for the resin, resulting in the lifting of the Mo film. Considering this, Fig. 3(a) clearly shows the thermal effusivity distribution of the sample particle. The particles on the left-hand side of the measurement area had a very low thermal effusivity of approximately 0–0.50 $kJs^{-0.5}m^{-2}K^{-1}$. In contrast, the thermal effusivity of the particles in the region on the right was 3 $kJs^{-0.5}m^{-2}K^{-1}$. This difference could be attributed to the fact that the area on the left contained more resin and fewer particles. This might have resulted in the following: (i) the difference between the hardness of the sample and the resin caused the polishing state to be different; therefore, the heights of the respective surfaces were different, and the thickness of the Mo film was not uniform; and (ii) the small thermal effusivity of the parts covered with resin caused the Mo film to lift during the measurement. Figure 3 (b) was taken after the thermal effusivity measurement. The epoxy resin out of the measured area showed dark gray, while the epoxy resin left

upper part in the measured area showed black color. The measurement was conducted along the longitudinal direction in the figure. The dark gray color region of the resin would be caused by the heating. In more detail, the simulations, such as the finite element method, should be conducted based on the experimental conditions and the thermophysical properties of the resin and molybdenum. In other words, the temperature rise during measurement needs to be predicted to estimate the possibility of resin evaporation and Mo participation. This should be a future challenge.

No such influence of the resin was observed on the right-hand side of the measurement area, as shown in Fig. 3(b). However, the thermal effusivity of particle 1 is approximately 5 $kJs^{-0.5}m^{-2}K^{-1}$, whereas that of particle 2 is approximately 6 $kJs^{-0.5}m^{-2}K^{-1}$, thereby setting up an approximate difference of 1 $kJs^{-0.5}m^{-2}K^{-1}$ since the detection laser was out of focus in the second half of the measurement when the measurement area was as large as 1000 μm × 1000 μm.

Therefore, instead of acquiring measurements from a large area, the measurements were obtained by focusing on each particle and considering a small area that included particles 1–4. Fig. 4 shows the results together with the SEM images acquired after the measurements. Compared to Fig. 3, which shows a large area, the results in Fig. 4 show that the thermal effusivity is more consistent when individual particles are measured. Moreover, when examined with BEI, uniform values were obtained in areas other than the edges of the particles, cracks, and holes. In areas close to these defects, a large apparent value was measured, which could be due to the different thicknesses of the Mo film compared with those in the interior or lifting of the Mo film. Similar thermal effusivity values were observed for particles 1–4, which indicated that the thermal effusivity of fayalite was approximately 4 $kJs^{-0.5}m^{-2}K^{-1}$.

The thermal effusivity of fayalite was determined more precisely based on the measurement results shown in Fig. 4 by applying probability density analysis. Figs. 5(a)–(c) show the probability density distribution of particles 1–4 and the results fitted to a normal distribution. The maximum probability density value was found at a smaller thermal effusivity around 3.5–4 $kJs^{-0.5}m^{-2}K^{-1}$. The larger thermal effusivity was found close to the defects, such as the edges of the particles or cracks. Therefore, the measured thermal effusivity was analyzed again, assuming the derived values comprised a mixture of those from fayalite and others that were affected by defects. A Gaussian mixture in scikit-learn and a machine-learning library in Python were adopted to estimate the mixture of normal distributions. Two mixed normal distributions were assumed: fayalite and the effect of defects. Fig. 5(d) shows the analysis results for all the measured values. Gaussian 1 is for fayalite, and Gaussian 2 is for the values affected by defects. The mean thermal effusivity of Gaussian 1 was close to the maximum value of the histogram.

The uncertainty for the measurement of the thermal effusivity of fayalite was analyzed according to the guide to the expression of uncertainty in measurement (GUM) [28], as shown in Table 2. The major sources of uncertainty are measurements of phase delay and thickness of Mo film. The sensitivity coefficient for phase difference and the thickness of Mo film was estimated from Eq. (1) under the condition that $d_f = 100$ nm, $\alpha_f = 4.59 \times 10^{-6}$ ($C_f\rho_f = 2.29 \times 10^6$ and $\lambda_f = 10.5$ $Wm^{-1}K^{-1}$ [25]) and $b_s = 4.14$ $kJs^{-0.5}m^{-2}K^{-1}$. The repeatability of phase difference was calculated from the estimated standard deviation of the 10 times measurements as 0.5°. The accuracy of phase delay measurement was estimated from that the resolution of phase delay was 0.0001° assuming the uniform distribution. The accuracy of the thickness of Mo film was estimated 1 nm, and a uniform distribution was assumed. The thickness of Mo film changes from position to position, which could change 16 nm in an area of 20 μm × 20 μm [24]. The standard uncertainty was estimated assuming the triangle distribution. In addition, the repeatability of measurement of the thermal effusivity was also evaluated from the standard deviation of Gaussian 1 (= 580 $kJs^{-0.5}m^{-2}K^{-1}$) and the number of analyzed data (= 1595). Finally, the combined standard uncertainty for the measurement of thermal effusivity was calculated to be 0.084 $kJs^{-0.5}m^{-2}K^{-1}$, resulting in 4.1 ± 0.2 $kJs^{-0.5}m^{-2}K^{-1}$with the coverage factor $k = 2$. The thermal conductivity was calculated as 6.0 ± 0.5 $Wm^{-1}K^{-1}$ using Eq. (5) based on the measured thermal effusivity and literature values of the density and specific heat of fayalite [29, 30], which were previously reported as 4.392 gcm^{-3} and 132.899 JK^{-1} mol^{-1}, respectively.

As indicated in section 2.1, the analytical model, *i.e.*, one-dimensional heat flow, can be applied for the sample with thermal effusivity smaller than 5 $kJs^{-0.5}m^{-2}K^{-1}$ and volumetric heat capacity larger than 2.5×10^6 $Jm^{-3}K^{-1}$. The volumetric heat capacity of fayalite is calculated to be 2.86×10^6 $Jm^{-3}K^{-1}$ from the literature value of density and specific heat [29, 30]. Thus, the sample condition was confirmed to satisfy the requirement for one-dimensional analysis by MDTR applied in this study.

The thermal diffusion length (l) for the measurement was determined from the thermal effusivity obtained in this study based on the following equation:

$$l = \sqrt{\frac{\alpha}{\pi f}} = \frac{b}{\rho C}\sqrt{\frac{1}{\pi f}} \tag{7}$$

The period of the heating laser in the measurements was set to $f = 1$ MHz; therefore, l was estimated as 0.8 μm. The samples used in this study were prepared by polishing fayalite-sized particles (150–180 μm) embedded in resin. The finite thickness of the polished particles did not affect the measurements, considering the initial particle size was sufficiently larger compared to the thermal diffusion length. Therefore, the thermal effusivity value measured in this study is considered to represent the bulk value.

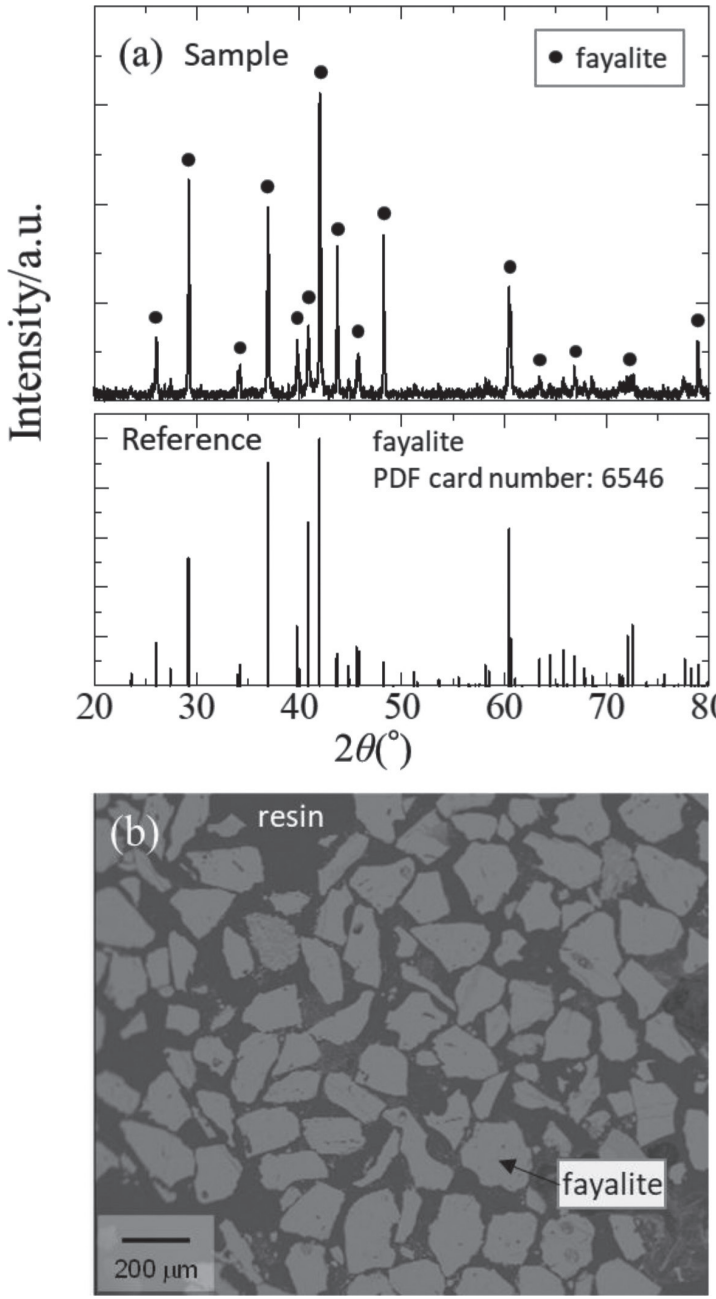

FIGURE 2
Results for sample analysis: (a) XRD profiles for powdered fayalite sample and the reference (PDF card number: 6546), where 2θ represents diffraction angle, and (b) SEM image for fayalite sample mounted in epoxy resin.

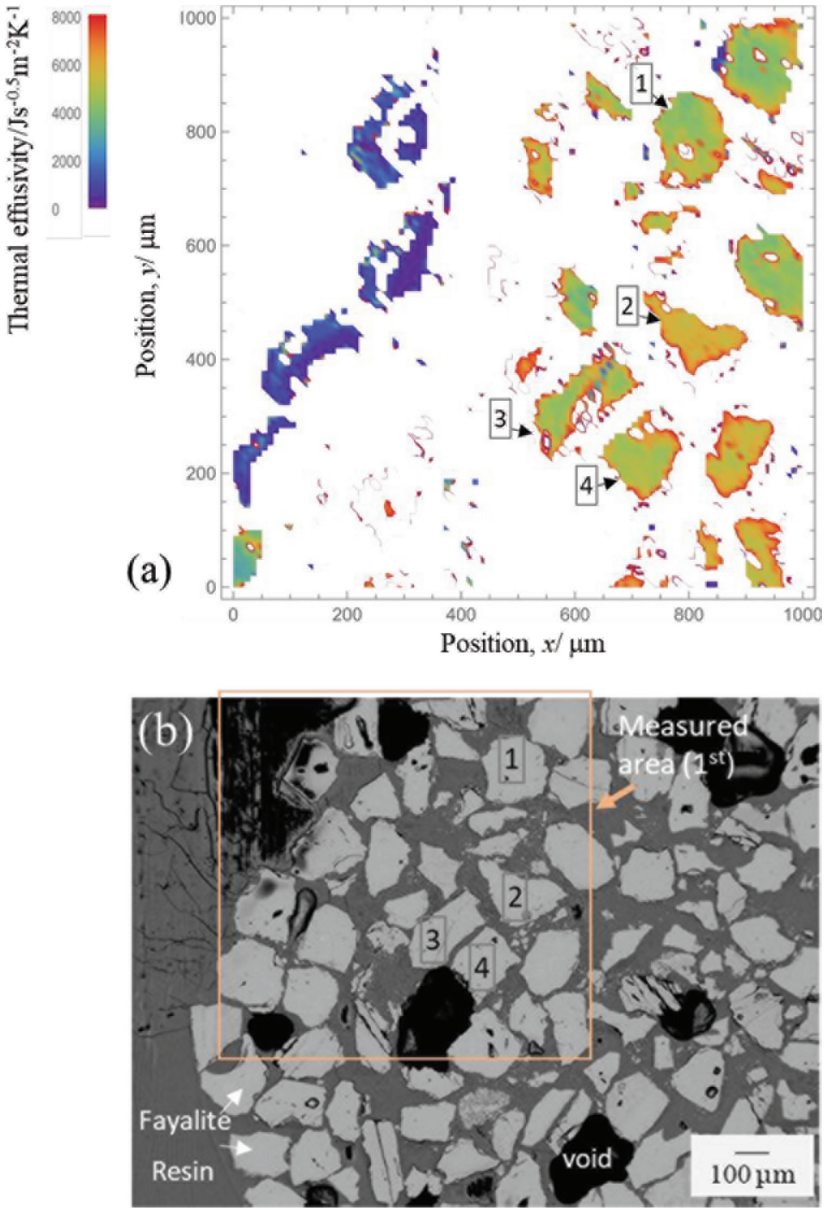

FIGURE 3
(a) Distribution of thermal effusivity measured for 1000 × 1000 µm^2 area and (b) corresponding BEI.

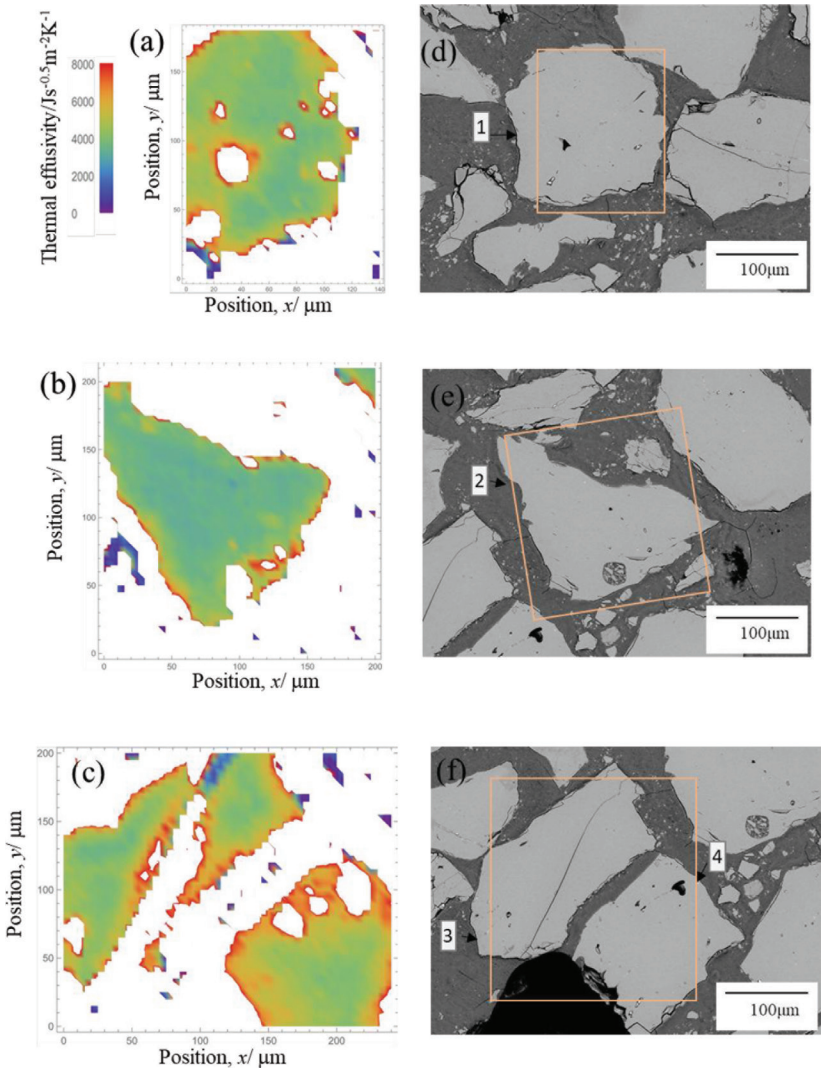

FIGURE 4
Thermal effusivity distribution and corresponding BET images for particle 1; (a) and (b), for particle 2; (c) and (d), and for particles 3 and 4; (e) and (f).

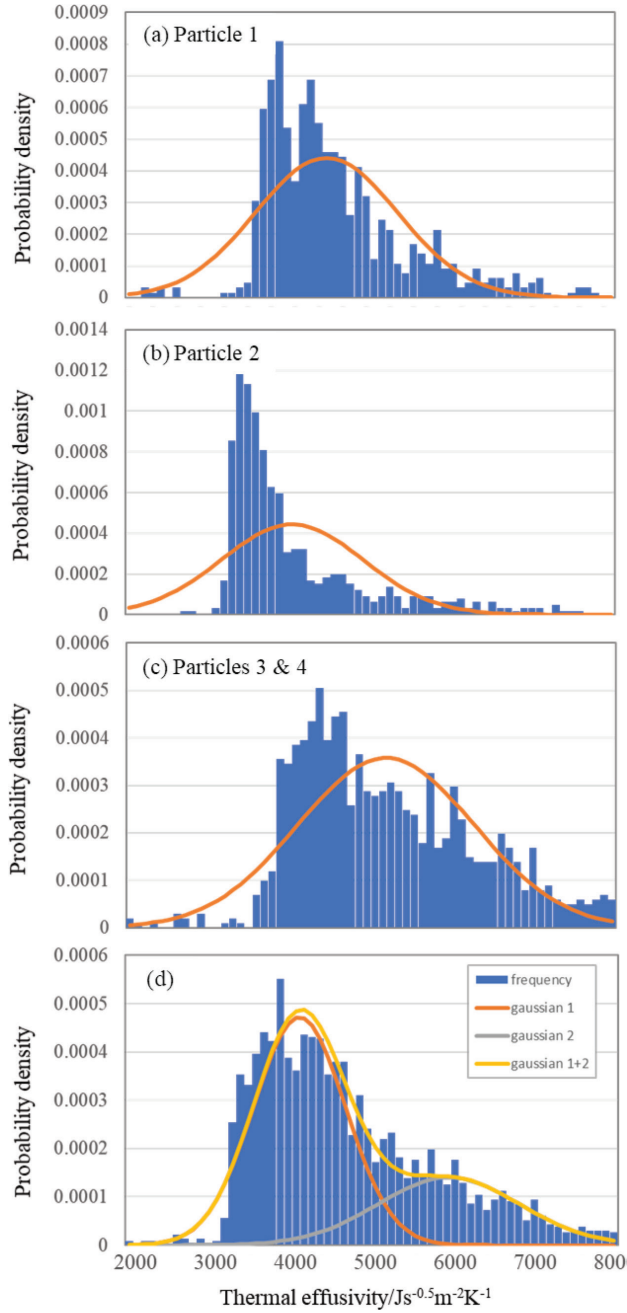

FIGURE 5
Probability density distribution calculated for (a) particle 1, (b) particle 2 and (c) particles 3 & 4, and (d) analysis result for two gaussian model.

TABLE 2
Uncertainty budget of the measurement of thermal effusivity for fayalite

Factor, x_i	**Type**	**Standard uncertainty, $u(x_i)$**	**Units**	**Sensitivity coefficient, c_i**
b		14.5	$Js^{-0.5}m^{-2}K^{-1}$	1
Repeatability	A	14.5	$Js^{-0.5}m^{-2}K^{-1}$	
Phase delay		0.158	°	507.5
Repeatability	A	0.158	°	
Accuracy of measurement	B	0.577×10^{-5}	°	
Thickness of Mo film		3.32	nm	6.75
Accuracy	B	0.577	nm	
Distribution	A	3.27	nm	
Combined standard uncertainty		$u_c(b) = \sqrt{\sum[c_i u(x_i)]^2} = 84.6$	$Js^{-0.5}m^{-2}K^{-1}$	

3.2 Comparison with reported values

Fig. 6 shows the thermal conductivity of olivines, fayalite-forsterite system, as a function of the percentage of forsterite (Mg_2SiO_4). Kingery et al. [31] measured the thermal conductivity of synthesized sintered forsterite. An equation eliminated the porosity effect. The thermal conductivity at 25 °C was estimated by assuming that the thermal conductivity is proportional to the reciprocal of temperature. Takeda *et al.* [1] reported that the thermal conductivity of a sintered sample of synthesized fayalite was 3 $Wm^{-1}K^{-1}$ at room temperature. The density of the sample used was 4.08 gcm^{-3}, which indicated that the porosity of the sample was estimated to be 6% [29]. Because the pores affected the reported values, the measured thermal conductivity was lower than the corresponding bulk value. It is reasonable to assume that the measured value in this study was larger than that reported by Takeda *et al.*

Horai reported the thermal conductivity of olivines, including fayalite-rich olivine (96%Fe_2SiO_4-4%Mg_2SiO_4) with a thermal conductivity of 3.16 $Wm^{-1}K^{-1}$ [2, 3]. A natural mineral was used as the sample. The needle-probe method was applied for the thermal conductivity measurement, and the sample used was powdered rocks (particle size less than 0.05 mm) immersed in water. The thermal conductivity of the rock was calculated from the volume fractions of the sample and water to eliminate the effect of water on the measured value. The uncertainty of their measurements was reported to be approximately 10%. The slight differences in thermal conductivity between this study and fayalite-rich olivine (96%Fe_2SiO_4-4%Mg_2SiO_4) can be attributed to the sample composition; the impurities scatter phonon. Fig. 6 also shows that the thermal conductivity of fayalite is almost the same as that of forsterite, and the value is larger than that of olivine reported by Horai. The natural mineral was used as an olivine

sample by Horai; other components could be included in the sample, resulting in a smaller thermal conductivity.

The thermal conductivities of the wüstite ($Fe_{1-x}O$) scale and wüstite-dominated scale prepared by oxidation in the air have been reported to be 2.17 $Wm^{-1}K^{-1}$ and 1.6 $Wm^{-1}K^{-1}$, respectively [7, 8, 32], whereas the thermal conductivity of fayalite was found to be larger than these values. It has been explained that the thermal conductivity of wüstite is smaller than that of other oxides, such as NiO and CaO, owing to the point defects of Fe ions [13]. Fayalite is also a non-stoichiometric compound, such as wüstite [33], and as a complex oxide, it is expected to have a lower thermal conductivity owing to phonon scattering. However, in practice, wüstite has lower thermal conductivity than fayalite due to the large number of Fe ion defects introduced in wüstite, which act as phonon scattering centers.

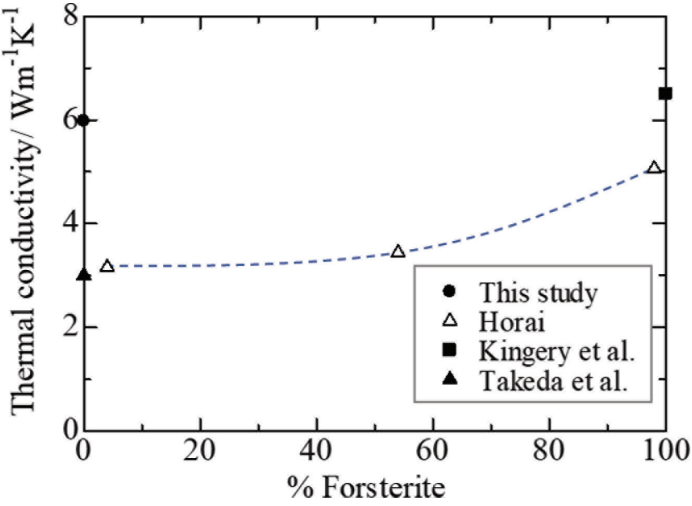

FIGURE 6
Thermal conductivity of fayalite-forsterite system as a function of percentage of forsterite [1, 2, 31].

3.3 Evaluation of thermal conductivity of the Si-rich layer in the oxide scale and heat resistance of the oxide scale

The results of this study were used to estimate the thermal resistance of an oxide scale containing fayalite based on the structure of the oxide scale formed on a thick steel plate. Fig. 7(a) shows a cross-sectional SEM image of the oxide scale formed on the thick steel plate. The image shows layers containing Si, wüstite, and magnetite (Fe_3O_4) from the steel side with a total thickness of approximately 44 μm. The thickness of the Si-rich layer is not uniform. Magnetite is also present in the wüstite layer owing to the thermal decomposition of $Fe_{1-x}O$ during cooling [34–36] or progressive oxidation by

oxygen through the cracks. Fig. 7(b) shows a magnified image of the Si-rich layer comprising pores and oxides that are thought to be a mixture of fayalite and wüstite; lighter areas indicate wüstite and darker areas indicate fayalite [5]. In the previous study [37], the Si-rich layer was thin, and pores were not found, while other reports also have shown that Si-rich layers contain pores [38–40] and fayalite and wüstite. Fig. 7(a) agrees with the latter case. The reason for forming uneven Si-rich layer thickness was unknown; the steel or oxide scale temperature was not considered uniform in the production process. There are several possibilities to cause uneven cooling of steel: the rolling contact during hot-rolling, cooling by high-pressure water during descaling, or cooling water after the hot-rolling.

As the thickness of the Si-rich layer is uneven, its thickness distribution needs to be investigated in the future, e.g., using tomography. Here, the effective thermal conductivity of the oxide layer has been roughly evaluated to clarify the effect of the unevenness of the Si-rich layer. Heat is transferred from the steel to the outer gas phase via the oxide scale when the hot steel plate is cooled by water. The total heat resistance of the oxide scale is estimated as follows:

$$\begin{aligned} R_{\text{total}} &= R_{\text{Si-layer}} + R_{\text{wüstite}} + R_{\text{magnetite}} \\ &= \frac{d_{\text{Si-layer}}}{\lambda_{\text{Si-layer}}} + \frac{d_{\text{wüstite}}}{\lambda_{\text{wüstite}}} + \frac{d_{\text{magnetite}}}{\lambda_{\text{magnetite}}} \end{aligned} \tag{8}$$

where R is the heat resistance, and the subscripts total, Si-layer, wüstite, and magnetite denote the total, Si-rich, wüstite, and magnetite layers, respectively. Each term on the right-hand side of Eq. (8) represents the heat resistance of each layer. The thickness of each layer can be measured from the image, such as Fig. 7(a), and literature values are available for the thermal conductivity of wüstite and magnetite. Here, the thermal conductivity of the Si-rich layer is estimated as follows. The Si-rich layer in Fig. 7(b) seems to have a layered structure composed of fayalite, wüstite, and pore. Each phase in the Si-rich layer appeared to exist across the heat flow. The effective thermal conductivity (λ_{eff}) of a laminated material comprising three phases in the lamination direction is given as [17]:

$$\frac{1}{\lambda_{\text{eff}}} = \frac{V_1}{\lambda_1} + \frac{V_2}{\lambda_2} + \frac{V_3}{\lambda_3} \tag{9}$$

where V is the volume fraction, and the subscripts indicate each phase. The thermal conductivity of the Si-rich layer ($\lambda_{\text{Si-layer}}$) was calculated based on the above Equation, where λ_{eff} was replaced by $\lambda_{\text{Si-layer,}}$ the existing phases were wüstite, fayalite, and pores, and the volume fraction was replaced by area fraction. As shown in Fig. 7(a), the thickness of the Si-rich layer was not uniform. The oxide scale in Fig. 7(a) was divided into four parts, each part having a width of 30 μm, as expressed by Fig. 7(a)–I to Fig. 7(a)–IV from left to right, to obtain

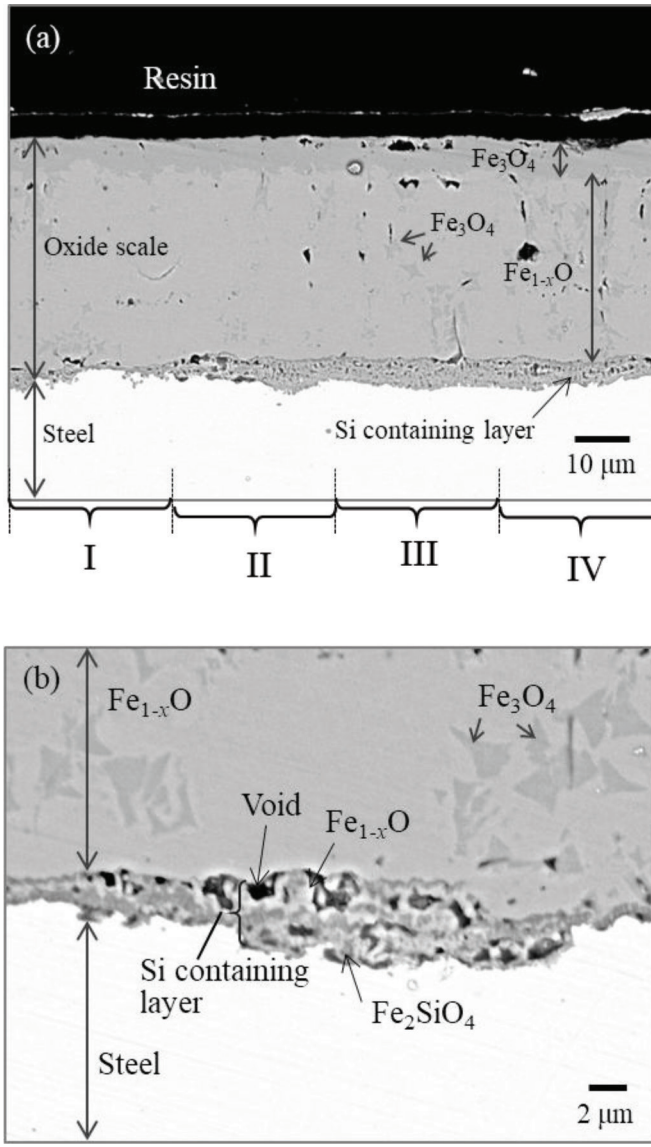

FIGURE 7
(a) Cross-sectional BEI for oxide scale formed and heavy steel plate and (b) magnified image for the interface between steel and oxide scale.

the possible error range. The average thickness of the Si-rich layer and the ratio of the three phases were analyzed by image processing [41], with lighter areas indicating wüstite, darker areas showing fayalite, and black areas indicating pores [5]. The results are presented in Table 3. The ratios of the existing phases

in the Si-rich layer were 0.51 ± 0.06 for wüstite, 0.35 ± 0.08 for fayalite, and 0.13 ± 0.05 for pore, respectively, where the error is the standard deviation. The result for Fig. 7(a)–I have less pore ratio in the Si-rich layer than in other portions, and the thickness of the Si-rich layer is the thinnest. It can be considered that the Si-rich layer contains more pores as it grows. The thermal conductivity of the Si-rich layer was calculated based on Equation (9), where the thermal conductivities of 0.0256 $Wm^{-1}K^{-1}$ [42] and 2.17 $Wm^{-1}K^{-1}$ [11, 32] and 6.0 $Wm^{-1}K^{-1}$ were used for the air, wüstite, and fayalite, respectively, at room temperature. The thermal conductivity of the Si-rich layer formed on the thick steel plate was one order of magnitude lower than that of the constituent oxides. It was strongly affected by the pores, which indicates that accurate porosity estimation and thickness are necessary to calculate effective thermal conductivity. The same results were also reported previously [31, 43, 44].

Table 3 also lists the calculated thermal resistance of the oxide scale. A large thermal resistance was observed when the thickness of the Si-rich layer and the pore ratio were large. The total heat resistance of 4.8–34.4 × 10^{-6} m^2KW^{-1} is equivalent to steel with a thickness of 0.2–1.8 mm, where the thermal conductivity of the steel was assumed to be 51.9 $Wm^{-1}K^{-1}$ [46]. Table 3 also shows that the thermal resistance of the oxide scale varies from place to place; hence, the cooling rate of steel also varies. A simulation would be required to evaluate the temperature distribution in steel and the oxide scale during cooling based on the structural data, such as the thickness distribution of the Si-rich layer, *etc.*

TABLE 3
Calculation results for contribution of each phase to the total heat resistance of the oxide scale

Oxide sclae	**Fig. 7(a)–I**	**Fig. 7(a)–II**	**Fig. 7(a)–III**	**Fig. 7(a)–IV**
Si-rich layer				
Average thickness/mm	2.1	4.8	5.3	4.7
Phase ratio of wüstite: fayalite: pore	0.56 : 0.39 : 0.05	0.60 : 0.22 : 0.18	0.54 : 0.36 : 0.10	0.46 : 0.41 : 0.13
Thermal conductivity/ $Wm^{-1}K^{-1}$	0.44	0.14	0.23	0.19
Wüstite layer				
Thickness/mm		34		
Thermal conductivity/ $Wm^{-1}K^{-1}$		2.17 [11, 32]		
Magnetite layer				
Thickness/mm		5		
Thermal conductivity/ $Wm^{-1}K^{-1}$		3.5 [45]		
Thermal resistance of oxide scale, $R_{total}/10^{-6}m^2KW^{-1}$	4.8	34.4	23.4	19.2
$R_{si\text{-}layer}/R_{total}$	0.22	0.66	0.58	0.58

*The Si-rich layer in Fig. 7(a) was divided into four parts, *i.e.,* every 30 μm width. The Si-rich layer parts were named Fig. 7(a)–I to Fig. 7(a)–IV from left to right.

4 CONCLUSIONS

This study determined the thermal effusivity/conductivity for fayalite particles with diameters smaller than 180 μm. The modulated thermoreflectance microscopy was applied for the measurement because the technique can derive the thermal properties for a small area of around 10 μm. The thermal effusivity of fayalite was found to be 4.1 ± 0.2 $kJK^{-1}m^{-2}s^{-0.5}$. This value produced a fayalite thermal conductivity of 6.0 ± 0.5 $Wm^{-1}K^{-1}$, which is larger than the $Fe_{1-x}O$ scale. The thermal conductivity of fayalite is almost the same as that for forsterite, another constituent of olivine, and the value is larger than that for olivine (solid solution of fayalite and forsterite).

Based on these results, we estimated the thermal conductivity of the Si-rich layer in the oxide scale formed on the thick steel plate. The oxide scale consisted of a Si-rich layer, a wüstite layer, and a magnetite layer. The last two layers show almost uniform thickness, while the thickness of the Si-rich layer was uneven. The Si-rich layer composes of fayalite, wustite, and pore. The effective thermal conductivity of the Si-rich layer and oxide scale was calculated from the observation result of the oxide scale. The result indicates that the thermal conductivity of the oxide scale is strongly affected by the thickness of the Si-rich layer because the layer contains many pores. Furthermore, the contribution of the Si-rich layer to the heat resistance of the oxide scale was found to be significantly large compared to the thickness.

ACKNOWLEDGMENTS

This research was partially supported by JSPS KAKENHI Number 21K04735 and an Amada Foundation Grant-in-Aid for General Research and Development. The authors appreciate the contribution of Prof. Endo at Teikyo Heisei University, Japan, for support with the Python analysis. We would like to thank Editage (www.editage.com) for the English language editing.

REFERENCES

[1] Takeda, M., Onishi, T., Nakakubo, S., Fujimoto, *S. Mater. Trans.,* **50** (2009), 2242–2246. https://doi.org/10.2320/matertrans.M2009097
[2] Horai, *K. J. Geophys. Res.* **76**, (1971), 1278–1308. https://doi.org/10.1029/JB076i005p01278
[3] Čermák, V., Rybach, L., Landolt-Börnstein, Vol 1a, Group, Springer, Berlin. **5**, (1982), 305–343.
[4] Tuck, C.W. *Corros. Sci.*, **5**, (1965), 631–643. https://doi.org/10.1016/S0010-938X(65)90189-7
[5] Smeltzer, W., Morris, L.A., Logani, R.C. Can. Metall. Q. **9,** (1970), 513–519. https://doi.org/10.1179/cmq.1970.9.4.513
[6] Logani, R.C., Smeltzer, W.W. *Oxid. Met.* **3,** (1971), 15–32. https://doi.org/10.1007/BF00604737
[7] Yanagihara, K., Suzuki, S., Yamazaki, S. *Oxid. Met.* **57,** (2002), 281–296. https://doi.org/10.1023/A:1014826318890

[8] Endo, R., Yagi, T., Ueda, M., Susa, M. *ISIJ Int.* **54,** (2014), 2084–2088. https://doi.org/10.2355/isijinternational.54.2084
[9] Li, M., Endo, R., Akoshima, M.. Susa, M. *ISIJ Int.* **57,** (2017), 2097–2106. https://doi.org/10.2355/isijinternational.ISIJINT-2017-301
[10] Yang, Y., Watanabe, H., Ueda, M., Hayashi, M., Susa, M., Endo, R. *ISIJ Int.* **58,** (2018), 2186–2190. https://doi.org/10.2355/isijinternational.ISIJINT-2018-380
[11] Li, M., Endo, R., Akoshima, M., Tanei, H., Okada, H., Susa, M. *ISIJ Int.* **59,** (2019), 398–403. https://doi.org/10.2355/isijinternational.ISIJINT-2018-553
[12] Endo, R., Hayashi, H., Li, M., Akoshima, M., Okada, H., Tanei, H., Hayashi, M., Susa, M. *ISIJ Int.* **60,** (2020), 2773–2779. https://doi.org/10.2355/isijinternational.ISIJINT-2020-163
[13] Yang, Y., Watanabe, H., Akoshima, M., Hayashi, M., Susa, M., Tanei, H., Okada, H., Endo, R. *ISIJ Int.* **61,** (2021), 26–32. https://doi.org/10.2355/isijinternational.ISIJINT-2019-635
[14] Bowen, N. L., Schairer, J. F. *Am. J. Sci.,* s. 5–24, (1932), 177–213. https://doi.org/10.2475/ajs.s5-24.141.177
[15] Akiyama, T., Ohta, H., Takahashi, R., Waseda, Y., Yagi, J. *ISIJ Int.* **32** (1992) 829–837. https://doi.org/10.2355/isijinternational.32.829
[16] Dul'nev, G. N., Zarichnyak, Y. P. *J. Eng. Phys.* **12,** (1967), 215–219. https://doi.org/10.1007/BF00836519
[17] Nayfeh A. H. *J. Appl. Mech.,* **42,** (1975), 399. https://doi.org/10.1115/1.3423589
[18] Chen, W., Feng, Y., Qiu, L., Zhang X. *Int. J. Heat Mass Transf.* **154**, (2020), 119750-1–5 https://doi.org/10.1016/j.ijheatmasstransfer.2020.119750
[19] Liu, Z., Feng, Y., Qiu, L. *Appl. Phys. Lett.* **120**, (2022), 113506-1–6. https://doi.org/10.1063/5.0080083
[20] Hatori, K., Taketoshi, N., Baba, T., Ohta, H. *Rev. Sci. Instrum.* **76** (2005). https://doi.org/10.1063/1.2130333, http://www.ncbi.nlm.nih.gov/pubmed/114901
[21] Okamoto, Y., Okada, R., Nemoto, T., Ohta, H., Takiguchi, H. *Int. J. Thermophys.* **33** (2012), 1219–1227. https://doi.org/10.1007/s10765-012-1249-2
[22] Ohta, H., Hatori, K., Matsui, G., Yagi, T., Miyake, S., Okamura, T., Endoh, R., Okada, R., Morishita, K., Yokoyama, S., Taguchi, K., Kato H. *Meas. Sci. Technol.* **27,** (2016). https://doi.org/10.1088/0957-0233/27/11/115002, http://www.ncbi.nlm.nih.gov/pubmed/115002
[23] Miyake, S., Matsui, G., Ohta, H., Hatori, K., Taguchi, K., Yamamoto, S., *Meas. Sci. Technol.* **28**, (2017), https://doi.org/10.1088/1361-6501/aa72d0
[24] Nishi, T., Yamamoto, S., Okawa, M., Hatori, K., Ikeda, T., Ohta, H. *Thermochim. Acta.* **659,** (2018), 39–43. https://doi.org/10.1016/j.tca.2017.11.004 [21].
[25] Endo, R., Suganuma, Y., Endo, K., Nishi, T., Ohta, H., Tachikawa, S. *Int. J. Thermophys.* **43,** (2022), 1–18. https://doi.org/10.1007/s10765-022-03031-y
[26] Wolfram Research, Inc., Mathematica, Version 11, Champaign, IL (2017).
[27] Garrett, T. W., Rosenberg, H. M. J. Phys. D: Appl. Phys., **7** (1974) 1247–1258. https://doi.org/10.1088/0022-3727/7/9/311
[28] ISO/IEC Guide **98** (1995).
[29] Takei, H. *J. Cryst. Growth.* **43,** (1978), 463–468. https://doi.org/10.1016/0022-0248(78)90344-5
[30] Barin, I. Thermochemical Data of Pure Substances, third ed, Wiley Online Library Online Books. (Accessed 12 December 2020), p. 713, 1997.
[31] Kingery, W. D., Francl, J., Coble, R. L., Vasilos, T. *J. Am. Ceram. Soc.*, **37**, (1954), 107–110, https://doi.org/10.1111/j.1551-2916.1954.tb20109.x
[32] Shinohara, S., Endo, R., Watanabe, T., Hayashi, M., Tanei, H., Susa, M. *Tetsu-to-Hagane.* **107** (2021) 551–557. https://doi.org/10.2355/tetsutohagane.TETSU-2021-002
[33] Brinkmann, U., Laqua, W. *Phys. Chem. Minerals* **12,** (1985), 283–290. https://doi.org/10.1007/BF00310341
[34] Darken, L. S., Gurry, R.W. *J. Am. Chem. Soc.* **68** (1946) 798–816. https://doi.org/10.1021/ja01209a030
[35] Tanei, H., Kondo, Y. *ISIJ Int.* **57,** (2017), 506–510. https://doi.org/10.2355/isijinternational.ISIJINT-2016-552
[36] Tanei, H., Kondo, Y. *ISIJ Int.* **52,** (2012), 105–109. https://doi.org/10.2355/isijinternational.52.105
[37] Endo, R., Yagi, T., Ueda, M., Susa, M., *ISIJ Int.* **54**, (2014), 2084–2088. https://doi.org/10.2355/isijinternational.54.2084

[38] Nilsonthi, T. *Mater. Today Proc.* **5,** (2018), 9552–9559. https://doi.org/10.1016/j.matpr.2017.10.137
[39] He, B., Xu, G., Zhou, M.X., Yuan, Q. Metals. **6** (2016). https://doi.org/10.3390/met6060137
[40] Alaoui Mouayd, A., Koltsov, A., Sutter, E., Tribollet, B., *Mater. Chem. Phys.* **143**, (2014), 996–1004. https://doi.org/10.1016/j.matchemphys.2013.10.037
[41] Rasband, W. S. ImageJ, 1997–2012. https://imagej.nih.gov/ij/, U. S. National Institutes of Health, Bethesda, Maryland.
[42] National Astronomical Observatory of Japan, Thermal Conductivity of Air, Chronological Scientific Tables Premium, Maruzen. (Accessed 18 December 2021), 2021.
[43] Qiu, L., Yan, K., Feng, Y., Liu, X., Zhang, X. *Compos. Commun.* **27**, (2021), 100892-1–5, https://doi.org/10.1016/j.coco.2021.100892
[44] Jia, D., Kim, D. K., Kriven, W. M. J. Am. Ceram. Soc. **90**, (2007), 1760–1773. https://doi.org/10.1111/j.1551-2916.2007.01704.x
[45] Li, M., Akoshima, M., Endo, R., Ueda, M., Tanei, H., Susa, M. *ISIJ Int.* **62,** (2022), 275–277. https://doi.org/10.2355/isijinternational.ISIJINT-2021-326
[46] Japan Society of Thermophysical Properties, Thermophysical Properties, Handbook, Yokendo, Tokyo, 210 (in Japanese), 2008.